

# Unsupervised deep learning method for cell segmentation

Nizam Ud Din, Ji Yu\*

Center for Cell Analysis and Modeling, UConn Health

400 Farmington, Farmington, CT 06030, USA

\* corresponding author: [jyu@uchc.edu](mailto:jyu@uchc.edu)

## Abstract

Advances in the artificial neural network have made machine learning techniques increasingly more important in image analysis tasks. Recently, convolutional neural networks (CNN) have been applied to the problem of cell segmentation from microscopy images. However, previous methods used a supervised training paradigm in order to create an accurate segmentation model. This strategy requires a large amount of manually labeled cellular images, in which accurate segmentations at pixel level were produced by human operators. Generating training data is expensive and a major hindrance in the wider adoption of machine learning based methods for cell segmentation. Here we present an alternative strategy that uses unsupervised learning to train CNNs without any human-labeled data. We show that our method is able to produce accurate segmentation models. More importantly, the algorithm is applicable to both fluorescence and bright-field images, requiring no prior knowledge of signal characteristics and requires no tuning of parameters.

## 26 Introduction

27 Automated cellular segmentation from optical microscopy images is a critical task in  
 28 many biological researches that rely on single-cell analysis. Traditional approaches to cell  
 29 segmentation rely on manually-crafted feature definitions that allow the algorithmic recognition  
 30 of cellular area and cell border<sup>1,2</sup>. Unfortunately manual feature definitions are usually highly  
 31 context-specific and require task-dependent tuning to work well. For example, an algorithm that  
 32 is well-optimized for a specific membrane fluorescent marker will not work on images of a  
 33 different fluorescent marker, nor on bright field images. Switching to a different cell type (with  
 34 different morphological features), changing imaging modality (e.g., from epi-fluorescence to  
 35 confocal), or even imaging settings (e.g. changing the objective) often requires a  
 36 redesign/reoptimization of the segmentation algorithm. Therefore, there is a need for more  
 37 generic, “turn-key” solutions for this task.

38 Convolutional neural networks (CNN) have recently been shown to be highly efficient on  
 39 various kinds of image processing tasks, including semantic segmentation<sup>3-6</sup>. In particular,  
 40 various networks with an hourglass-shaped architecture (e.g., UNet) have achieved remarkable  
 41 pixel-level accuracy in segmentation of objects, including biological cells<sup>7-11</sup>. However, there are  
 42 two major problems that have prevented the adoption of CNNs in biological research. First,  
 43 while CNNs perform well in segmentation of a single cell, they often exhibit an  
 44 under-segmentation bias when processing crowded cell populations that contain many cells  
 45 adjacent to each other<sup>8</sup>. This makes them less desirable for common analytical tasks such as  
 46 high content screening, in which typically hundreds to thousands of cells need to be segmented  
 47 simultaneously from one image dataset. Second, and more importantly, to train a CNN for the  
 48 segmentation task, one needs a significant amount of manually labeled training images, in  
 49 which cell areas and/or cell boundaries are marked by human operators. Manually labeling is a

time-consuming and expensive process. As a result, CNN-based approach remains uncompetitive versus traditional segmentation approaches in real-life biological applications.

Here we propose a new CNN-based cell segmentation method that aims to solve the two problems described above. A key difference between our method and previous attempts at the CNN-based cell segmentation is that we use a marker-controlled segmentation algorithm, taking a note from conventional cell segmentation pipelines. Many conventional segmentation algorithms (e.g., watershed<sup>12</sup>) are known to have an over-segmentation bias when the images are contaminated with noise. One way to correct for the bias is to provide a set of specific marker positions, depicting the approximate locations of each cell. Indeed, it is a common practice to use two-channel imaging data for cell segmentation, one channel for imaging nucleus and the other for the whole cell. The nucleus images are useful for computing marker positions, and the whole cell images provide information for determining cell boundaries. This approach is used in some of the most widely-used cell segmentation softwares, such as Cell Profiler<sup>13</sup> and Ilastik<sup>14</sup>. The success of this approach derives partly from the fact that nucleus images have simple morphological features and therefore are relatively easy to analyze with traditional image processing algorithms. Nucleus identification and/or segmentation is a heavily researched topic; multiple algorithms exist in the literature with good performances<sup>15–19</sup>. The main challenge in cell segmentation is to devise reliable feature representations that can recognize cell boundaries with a high accuracy.

We propose to adopt the marker-controlled segmentation approach, but apply it to the CNN-based segmentation. We will first generate marker locations from nucleus images, but use a CNN to model cell features and produce accurate segmentation at the whole cell level. Unlike previous works on CNN segmentation, which use the networks to process the whole imaging field of view, we designed our network to perform segmentation on a smaller patch of the input image centered around the marker positions (Fig.1). This converts the multi-cell segmentation

75 problem to multiple single-cell segmentation problems, which in turn removes the  
76 undersegmentation bias as long as the nuclei markers were correctly computed. In addition, it is  
77 important to note that the “nucleus image” does not have to be one that is experimentally  
78 acquired. Instead, we will also demonstrate an alternative approach, in which we generate  
79 synthetic “nucleus images” from the normal whole cell images, by using a pretrained CNN  
80 model. This technique is similar to the method first demonstrated by Ounkomol et. al<sup>20</sup>, in which  
81 they showed that CNNs can be trained to map one image modality (e.g. bright-field image) to a  
82 different one (e.g. fluorescence images of plasma membrane, nucleus etc).

83 A more important consequence of the marker-controlled segmentation approach is that it  
84 allows us to devise a method to train segmentation CNNs (Fig. 1) in an unsupervised fashion,  
85 and thus avoiding the manual labeling of the training dataset. The key for achieving this is to  
86 design a custom objective function:

$$87 \quad -L(M, y^1, y^2, \dots, y^n) = \sum_{d_0, d_1} \sum_i y_{d_0, d_1}^i + \lambda \sum_{d_0, d_1} \sum_{i \neq j} y_{d_0, d_1}^i \cdot \log(1 - y_{d_0, d_1}^j) - \beta \sum_{d_0, d_1} \sum_i y_{d_0, d_1}^i (1 - M_{d_0, d_1}) \quad (1)$$

88 Here,  $y^i \in R^{k \times k}$  is the CNN output from  $i$ -th patch of the input image, which can be interpreted as  
89 the probability value for classifying each pixel within the patch to be one belonging to the cell.  
90 The summations over  $d_0, d_1$  are over all pixels in the input image, and the summations over  $i$  or  $j$   
91 are over all patches. Furthermore, we use the notation  $y_{d_0, d_1}^i$  to denote the value of  $y^i$  at a  
92 specific pixel location  $d_0, d_1$ . Since the individual CNN output covers only a small area of the  
93 entire image input, we assume a zero value when the index location  $d_0, d_1$  is outside the  
94 computed area, consistent with the probabilistic interpretation of  $y^i$ . Finally,  $M$  is a binary mask  
95 indicating the area of all cells, which can be generated from the input data with a graph cut  
96 algorithm. The goal is to train CNN until the loss function  $L$  is minimized. Since the loss function

is designed to be fully differentiable, we can use the standard stochastic optimization<sup>21</sup> and back-propagation technique to achieve the goal in a manner similar to supervised training.

The objective function contains three terms. The first term is optimized by including as many pixels as possible in the segmented results. This is balanced by the second term, which penalizes any overlaps of segmented pixels from different patches. Finally, the third term gives additional penalties if the segmented pixels exceed the masked area, i.e, it prevents the model from including the background pixels in the segmentation. The two hyper parameters,  $\lambda$  and  $\beta$ , control the relative weight of the penalty terms. Because the CNN model processes each individual patch independently, when segmenting one cell, the network is unaware of the results from adjacent patches. Therefore, the loss function is minimized only after the network has “learned” meaningful semantic features from the images, which in turn would hopefully result in correct segmentations.

## Results

We implemented the proposed algorithm using the TensorFlow computational framework<sup>22</sup> and tested its efficacy on both immunofluorescence (anti-phosphotyrosine (pY) ) and bright-field microscopy image data. In addition, to compute marker locations, we obtained nucleus images by staining cells with DNA binding dye DAPI. Traditional segmentation algorithms generally do not work on bright-field images and often work poorly on noisy signals such as those in immunofluorescence data. Therefore, our datasets serve as stress tests of the segmentation algorithm by presenting more challenging use cases.

We train modified UNets (Fig. S1) with the acquired images to generate a segmentation model. We first used the Cell Profiler software to analyze the nucleus image and computed the locations of each detected nucleus as the markers, which in turn were used to produce image patches (64x64 pixels), each centered around a marker location. The patch size was chosen to

121 be larger than the size of a single cell, thus many patches have significant overlapping areas.  
 122 The image patches were used as the inputs to train the neural network by minimizing the loss  
 123 function  $L$ . The goal is to train the UNet to segment one single cell from each image patch.  
 124 However, CNN output is dependent on local information only, and is not aware of the absolute  
 125 positions of the pixel inputs. To ensure the segmentation apply to only one specific cell, we  
 126 encoded positional information in the input data by including a image of a Gaussian disk ( $\sigma =$   
 127 15) at the marker location as an additional input channel. On top of that, in order to ensure the  
 128 features learned about cells are symmetric according to image orientation, we randomly flip the  
 129 patches along two major axes. A corresponding reverse operation was performed on the  
 130 network output before the computation of the loss function. For each independent dataset input,  
 131 we optimize a separate segmentation model based on the same underlying network architect  
 132 and training procedure.

133         The training process is stable and reasonably efficient. The loss function value (Fig. S2)  
 134 decreases in a generally monotonic fashion until converging to a stable minimal value. The  
 135 overall process took between 3-6 minutes on a single computational node with a K80 GPU  
 136 (graphic processing unit), depending on the input. In addition, we quantified segmentation  
 137 accuracies by computing mean intersection over union (mIOU) between machine  
 138 segmentations and manual segmentations (more details below). We found that the  
 139 segmentation accuracy increases monotonically over the training process and reached a stable  
 140 maximum. Therefore, the training process did not exhibit overfitting defects, supporting the  
 141 validity of the loss function design for the segmentation purpose. After the loss function value  
 142 stabilized, we then integrated the single-patch outputs from the CNN to generate the  
 143 segmentation map for the whole field-of-view (Fig. 2) for both immunofluorescence input and  
 144 bright field input. A quick visual examination indicated that the algorithm yielded qualitatively  
 145 believable segmentations in both cases.

146 To evaluate the segmentation quality, we performed three different quantitations of the  
147 segmentation results. First we quantified pixel level segmentation accuracy. To do that, we  
148 manually segmented ~130 cells randomly picked from three experimental datasets. The manual  
149 segmentation is performed by examining all available inputs (immuno-fluorescence, bright-field,  
150 and nucleus images) to ensure the highest accuracy. We then compute mIOUs between  
151 algorithm outputs and manual segmentations (Table I). As expected, the modal accuracy was  
152 higher when the model had taken multi-channel data as input during training. The highest mIOU  
153 accuracy (0.825) was achieved when the model was trained with all available data  
154 (immuno-fluorescence, bright-field, and nucleus images); conversely training the models with  
155 only the bright-field images resulted in the lowest accuracy (0.701). Training with  
156 immuno-fluorescence images produced better models than training with bright-field images,  
157 which is consistent with the impression that the immuno-fluorescence data offers clearer visual  
158 cues of cell boundaries. Including the nucleus images in the model training, somewhat  
159 surprisingly, improved the model accuracy slightly. Furthermore, inclusion of the nucleus images  
160 increased the convergence speed of the training significantly(Fig. S2). This is probably because  
161 the model could (correctly) infer that a segmentation boundary should traverse through the gap  
162 between two nuclei. Thus the exact information provided by the nucleus images allows quicker  
163 learning of the semantic features from the cell images. Finally, for a baseline analysis, we  
164 performed cell segmentation on the immunofluorescence data using Cell Profiler, a well-known  
165 cell segmentation software (Table 1). Cell profiler offers several predefined algorithms for  
166 unsupervised segmentation, the best of which resulted in an mIOU value of 0.69, significantly  
167 worse than our CNN model on the same fluorescence data. Cell Profiler was not designed to  
168 perform segmentation on bright-field images, therefore no comparison was made for the  
169 segmentations of bright-field image data.

170           Next we evaluated the consistency of segmentation results on images of differential  
171 modalities. One advantage of our algorithm is that it does not assume a priori specific  
172 characteristics of the data, and instead try to “learn” the semantic features from the images  
173 themselves. As a result the same algorithm could perform segmentation on either the  
174 fluorescence images or the bright-field images (Fig. 2) without the need to change parameters.  
175 However, if the segmentation results were accurate, then the results should be similar, if not  
176 identical, on images representing the same sample, which we found to be the case (Fig. 2e)..  
177 Quantitatively, we found that the mIOU between two segmentation results, one on the anti-pY  
178 immunofluorescence images and the other on bright-field images, was  $0.74 \pm 0.017$ . The mIOU  
179 value increased to  $0.809 \pm 0.051$ , if the nucleus images were also included during the model  
180 training. Therefore the segmentation outputs on differential image modalities indeed yielded  
181 results similar to one other, further supporting the notion that the self-supervised training  
182 process allows the CNN to learn correct cellular features.

183           Additionally, we tested whether models trained with one image input can perform  
184 segmentation on a different image that it had not seen yet. If the unsupervised training  
185 procedure allows the model to learn semantic features, then we should reasonably expect the  
186 trained model to also be able to operate on a different image that is acquired in a similar  
187 manner. Indeed we found that a pre-trained model can segment an unseen image producing a  
188 segmentation similar to that of a “proper” model, which had previously seen the image (Fig. S3),  
189 with mIOU = 0.752 for anti-pY immunofluorescence images and mIOU = 0.772 for bright-field  
190 images.

191           Next, we explore the possibility of generating marker positions directly from the cellular  
192 images themselves (i.e, not requiring a nucleus image). While the existence of the nucleus  
193 image provides a convenient means to generate the marker locations, the requirement exerts  
194 extra experimental overhead. We hypothesized that marker locations can also be



195 computationally obtained, if we produce a CNN model that could produce a synthetic “nucleus”  
 196 image from a normal cellular image, e.g., a bright-field image of cells. We tested this idea by  
 197 first training a UNet to perform a mapping, either from the anti-pY immunofluorescence images  
 198 or from the bright-field images, to their respective nucleus images. It is important to note that our  
 199 goal is not to produce a realistic nucleus image, but to compute the mark locations. Thus the  
 200 model can be of relatively low resolution. Indeed, we found that a useful model can be obtained  
 201 with very little training data: i.e., two images of 1750x1750 pixels in our test. Fig. 4 shows  
 202 examples of synthetic nucleus images by applying pretrained models to new images the models  
 203 hadn’t seen. While these synthetic images were far from indistinguishable from real nucleus  
 204 images, they reproduced the nucleus positions with enough accuracy to allow computing marker  
 205 locations via a simple blob detection algorithm. The marker locations were then combined with  
 206 the original cellular images to train a segmentation model using the unsupervised procedure  
 207 outlined earlier.

208       To evaluate the accuracy of the segmentation based on this synthetic marker procedure,  
 209 we separately quantify two sources of errors. Firstly, the model generated synthetic markers did  
 210 not perfectly match each individual nucleus in the sample, which resulted in either missing  
 211 markers (false negative) or extra markers (false positive) at wrong locations (Fig. 4). We  
 212 compared the synthetic marker locations with experimental images of the nuclei and found that,  
 213 for markers generated from immunofluorescence images, the average false negative rate is  
 214  $1.8 \pm 0.3\%$  and the average false positive rate is  $2.2 \pm 0.3\%$ , and for markers generated from  
 215 bright-field images, the average false negative rate is  $2.1 \pm 0.2\%$  and the average false positive  
 216 rate is  $2.4 \pm 0.3\%$ . These two types of errors correspond to missing cells and over-segmentation  
 217 of cells, respectively, in the final segmentation results. Furthermore, the segmentation model  
 218 had additional segmentation error at pixel level, which we evaluated by comparing the single  
 219 cell segmentation results with manual segmentations on selected cells. We found the mIOU

value to be  $0.814 \pm 0.025$  for segmenting anti-pY immunofluorescence images and  $0.755 \pm 0.033$  for segmenting bright-field images. Interestingly, the segmentation errors produced here are not significantly different from the models trained with “correct” marker locations (i.e, using experimental nucleus images, see Table 1), indicating that the small amount of false-positive and false-negative errors in synthetic markers had little impact on the training of the segmentation models.

## Discussion

Cellular imaging based high content screening has become more widely used in biological and medical researches<sup>23,24</sup>. The ability to perform single cell segmentation accurately and in a cost-effective manner is of great importance both to the commercial interests and to the basic sciences of studying single cells. Currently, accurate segmentation often requires a tailored algorithm specific to a fixed imaging modality, labeling procedure and specific imaging settings. Deviation from an optimized protocol often resulted in lowered performances. In general, these requirements significantly limit the flexibility in experimental designs. Machine learning based methods, on the other hand, promise to be more flexible because they are able to learn correct semantic features directly from data. Indeed, we show here that a CNN based computation method can perform cell segmentation on inputs of vastly different signal characteristics. In comparison to conventional algorithm-based segmentation tools, our method has the advantage of having a higher accuracy and being applicable to various input signal modality without the need of parameter tuning. More importantly, unlike previous CNN based segmentation tools, our method does not require any human labeled “ground-truth” data for training, and instead rely on an unsupervised training procedure, alleviating a significant barrier in applying deep learning strategy to cell segmentation.

243           The key insight from our work is that a properly designed artificial intelligence model can  
 244 learn semantic features from unlabeled cell image data by processing and comparing multiple  
 245 small image patches. The general concept of patch learning was recently introduced by several  
 246 highly influential studies<sup>25,26</sup> of unsupervised machine learning. Most current works in this area,  
 247 however, are focusing on the spatial context between non-overlapping patches as a source of  
 248 free information for training the models. The training generally requires a large amount of input  
 249 data. On the other hand, cellular images produced in biology have significantly higher feature  
 250 density (i.e., they contain nothing but cells) than most natural images. We show that the unique  
 251 characteristics of cell images can be leveraged to reduce the training data required, to a single  
 252 input image in our case. Tailored to this task, our training method used overlapping image  
 253 patches and relied on the consistency between patches for training, resulting in a unique  
 254 algorithm for this task.

255           The accuracy of our method is the highest if the user also acquires nucleus images from  
 256 the sample, which allows computer generation of “markers” that signify the location of individual  
 257 cells. However, the experimental data is optional, as we show “synthetic” nucleus images can  
 258 be generated using a machine learning approach. The latter strategy does require pre-training  
 259 of a CNN, which in turn requires additional training data in the form of cellular image / nucleus  
 260 image pairs. We note that nominally this is a type of supervised learning, but the training  
 261 process does not require manually labeling of data, and uses experimentally acquired images  
 262 as the “ground truth” instead. The overhead involved in the training process is generally low -- in  
 263 our case, we showed that training with two pairs of images were sufficient to produce results  
 264 accurate enough for marker computation. However, the training is specific to the exact signal of  
 265 interest. Switching the cellular image to a different label would need retraining of the network. In  
 266 the end, users of the algorithm will decide which strategy (experimental vs synthetic nucleus  
 267 markers) is more compatible with the specific research goal at hand.

## 268 **Method**

269       *Cell culture and microscopy:* All experiments were performed using the human  
 270 squamous-cell carcinoma line A431. Cells were plated onto plasma cleaned cover glass and  
 271 grown to ~70% confluence in standard growth media. Cells were quickly washed once with PBS  
 272 and fixed with 4% paraformaldehyde for 20 min. Cells were then washed with PBS three times  
 273 for 5 min each, permeabilized in 1.5% Triton-X PBS for 10 min and washed with PBS three  
 274 times for 10 min each. Dishes were then blocked in 1.5% BSA PBS for 60 min at 4°C, incubated  
 275 with alexa647-labeled anti-pY (1:500 in blocking buffer) for 2 h while rocking at 4°C, washed  
 276 three times for 5 min in PBS, and imaged in PBS in presence of DAPI. Epi-fluorescence and  
 277 brightfield images were acquired on an inverted fluorescence microscope (Olympus IX73) with  
 278 an 20x objective. An area of 1.4x1.4 mm was imaged with a grid pattern for each sample,  
 279 resulting in stitched images of 1750x1750 pixels. The final images were stitched using the  
 280 stitching plugin available in the Fiji software. Datasets were collected from three sample  
 281 replicates.

282       *Model training.* We first obtain a list of marker positions according to the centroid  
 283 locations of nuclei, using Cell Profiler (for experimental nucleus images) or using a blob  
 284 detection algorithm (for synthetic nucleus images). Image patches were extracted from the  
 285 inputs, which were either anti-pY fluorescence images or bright-field images of cells. A modified  
 286 UNet, used as the engine for cell segmentation, was trained to minimize the custom loss  
 287 function (Eq 1) with fixed hyperparameter values of  $\lambda = 1$  and  $\beta = 15$ , using the adaptive  
 288 momentum estimation (ADAM) optimization algorithm. Typically, processing all available image  
 289 patches in one batch would exceed the memory capacity of a GPU, even if the patches are from  
 290 just one input image. Therefore, we limit each computational batch to patches within a 640x640  
 291 area of the input image and process the whole image in steps. Data augmentation was  
 292 implemented by randomly flipping and/or transposing the input patches. A corresponding

reverse operation was performed on the network output before the computation of the loss function. The network was trained until the loss function reaches a stable minimum. To integrate individual segmentation results from patches to yield the segmentation results for the whole field-of-view, each pixel was assigned to the cell with the highest probability output at that location. Pixels showing segmentation probabilities less than 0.5 from all patches were assigned as the background.

*Binary mask.* A binary mask was used during training to ensure that the segmentation of individual cells will not exceed the area covered by the cells. For fluorescence images, the binary mask is generated using the “Graph Cut”<sup>27</sup> plugin in the Fiji software, which implements the well-known graph-cut algorithm. The algorithm relies primarily on the gray value differences to separate the foreground from the background, but compensate for the over-segmentation by introducing a penalty for foreground/background boundaries. For bright-field images, the gray values are not useful for distinguishing the foreground from the background. Therefore, we first train a two-class RandomForest model using the “Weka Segmentation”<sup>28</sup> Fiji plugin. We used Gaussian filter, variance and laplacian values as feature inputs. We then performed a graph cut on the model’s probability output and used the results as the mask.

*Synthetic nucleus image.* The same UNet (Fig. S1) architecture was used as the base CNN model for producing synthetic nucleus images. The UNet models were trained with small datasets of either two immunofluorescence (anti-pY) images or two brightfield images. Each input image was paired with a nucleus image, which was thresholded and converted to binary images. The training was stopped when the cross-entropy loss between model output and the (binary) nucleus images reached the value of 0.15. The pre-trained model was applied to new input images to produce the synthetic nucleus images.

# **Code availability**

317           Current implementation of the segmentation algorithm is available as a github repository.

318 <https://github.com/jiyuuchc/cellcutter>

319

# References

1. Meijering, E. Cell Segmentation: 50 Years Down the Road [Life Sciences]. *IEEE Signal Processing Magazine* **29**, 140–145 (2012).
2. Deshmukh, B. S. & Mankar, V. H. Segmentation of Microscopic Images: A Survey. in *2014 International Conference on Electronic Systems, Signal Processing and Computing Technologies* 362–364 (2014). doi:10.1109/ICESC.2014.68.
3. Krizhevsky, A., Sutskever, I. & Hinton, G. E. ImageNet classification with deep convolutional neural networks. *Commun. ACM* **60**, 84–90 (2017).
4. Long, J., Shelhamer, E. & Darrell, T. Fully convolutional networks for semantic segmentation. in *2015 IEEE Conference on Computer Vision and Pattern Recognition (CVPR)* 3431–3440 (2015). doi:10.1109/CVPR.2015.7298965.
5. Ronneberger, O., Fischer, P. & Brox, T. U-Net: Convolutional Networks for Biomedical Image Segmentation. *arXiv:1505.04597 [cs]* (2015).
6. Liu, Y., Minh Nguyen, D., Deligiannis, N., Ding, W. & Munteanu, A. Hourglass-ShapeNetwork Based Semantic Segmentation for High Resolution Aerial Imagery. *Remote Sensing* **9**, 522 (2017).
7. Al-Kofahi, Y., Zaltsman, A., Graves, R., Marshall, W. & Rusu, M. A deep learning-based algorithm for 2-D cell segmentation in microscopy images. *BMC Bioinformatics* **19**, 365 (2018).
8. Cameron, W. D., Bennett, A. M., Bui, C. V., Chang, H. H. & Rocheleau, J. V. Leveraging multimodal microscopy to optimize deep learning models for cell segmentation. *APL Bioengineering* **5**, 016101 (2021).
9. Wang, W. *et al.* Learn to segment single cells with deep distance estimator and deep cell detector. *Computers in Biology and Medicine* **108**, 133–141 (2019).
10. Wollmann, T. *et al.* GRUU-Net: Integrated convolutional and gated recurrent neural network

for cell segmentation. *Medical Image Analysis* **56**, 68–79 (2019).

11. Wolny, A. *et al.* Accurate and versatile 3D segmentation of plant tissues at cellular resolution. *eLife* **9**, e57613 (2020).

12. Bertrand, G. On Topological Watersheds. *J Math Imaging Vis* **22**, 217–230 (2005).

13. Carpenter, A. E. *et al.* CellProfiler: image analysis software for identifying and quantifying cell phenotypes. *Genome Biology* **7**, R100 (2006).

14. Berg, S. *et al.* ilastik: interactive machine learning for (bio)image analysis. *Nature Methods* **16**, 1226–1232 (2019).

15. Wang, M. *et al.* Novel cell segmentation and online SVM for cell cycle phase identification in automated microscopy. *Bioinformatics* **24**, 94–101 (2008).

16. Sharif, J. M., Miswan, M. F., Ngadi, M. A., Salam, M. S. H. & bin Abdul Jamil, M. M. Red blood cell segmentation using masking and watershed algorithm: A preliminary study. in *2012 International Conference on Biomedical Engineering (ICoBE)* 258–262 (2012). doi:10.1109/ICoBE.2012.6179016.

17. Ulman, V. *et al.* An objective comparison of cell-tracking algorithms. *Nature Methods* **14**, 1141–1152 (2017).

18. Dzyubachyk, O., Niessen, W. & Meijering, E. Advanced level-set based multiple-cell segmentation and tracking in time-lapse fluorescence microscopy images. in *2008 5th IEEE International Symposium on Biomedical Imaging: From Nano to Macro* 185–188 (2008). doi:10.1109/ISBI.2008.4540963.

19. Al-Kofahi, Y., Lassoued, W., Lee, W. & Roysam, B. Improved Automatic Detection and Segmentation of Cell Nuclei in Histopathology Images. *IEEE Transactions on Biomedical Engineering* **57**, 841–852 (2010).

20. Ounkomol, C., Seshamani, S., Maleckar, M. M., Collman, F. & Johnson, G. R. Label-free prediction of three-dimensional fluorescence images from transmitted-light microscopy. *Nature Methods* **15**, 917–920 (2018).



371 21. Kingma, D. P. & Ba, J. Adam: A Method for Stochastic Optimization. *arXiv:1412.6980 [cs]*  
372 (2017).

373 22. Martín Abadi *et al.* *TensorFlow: Large-Scale Machine Learning on Heterogeneous Systems*.  
374 (2015).

375 23. Boutros, M., Heigwer, F. & Laufer, C. Microscopy-Based High-Content Screening. *Cell* **163**,  
376 1314–1325 (2015).

377 24. Zanella, F., Lorens, J. B. & Link, W. High content screening: seeing is believing. *Trends in*  
378 *Biotechnology* **28**, 237–245 (2010).

379 25. Doersch, C., Gupta, A. & Efros, A. A. Unsupervised Visual Representation Learning by  
380 Context Prediction. in 1422–1430 (2015).

381 26. Noroozi, M. & Favaro, P. Unsupervised Learning of Visual Representations by Solving  
382 Jigsaw Puzzles. in *Computer Vision – ECCV 2016* (eds. Leibe, B., Matas, J., Sebe, N. &  
383 Welling, M.) 69–84 (Springer International Publishing, 2016).  
384 doi:10.1007/978-3-319-46466-4\_5.

385 27. Boykov, Y. & Kolmogorov, V. An experimental comparison of min-cut/max- flow algorithms  
386 for energy minimization in vision. *IEEE Transactions on Pattern Analysis and Machine*  
387 *Intelligence* **26**, 1124–1137 (2004).

388 28. Arganda-Carreras, I. *et al.* Trainable Weka Segmentation: a machine learning tool for  
389 microscopy pixel classification. *Bioinformatics* **33**, 2424–2426 (2017).

390

391

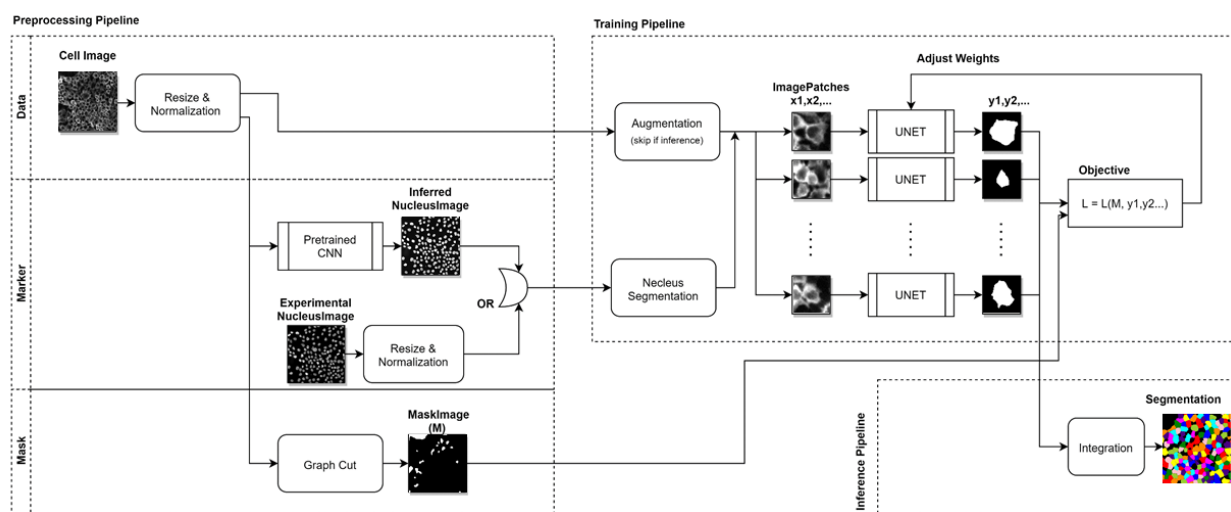


**Figure 1.** Schematic outline of the CNN segmentation algorithm. The overall process comprises three components: the preprocessing pipeline, which computes the marker location and image mask from the inputs, the training pipeline which extract image patches to train a CNN model for segmentation, and the integration pipeline that takes the single patch output from the CNN and create whole-field segmentation results.

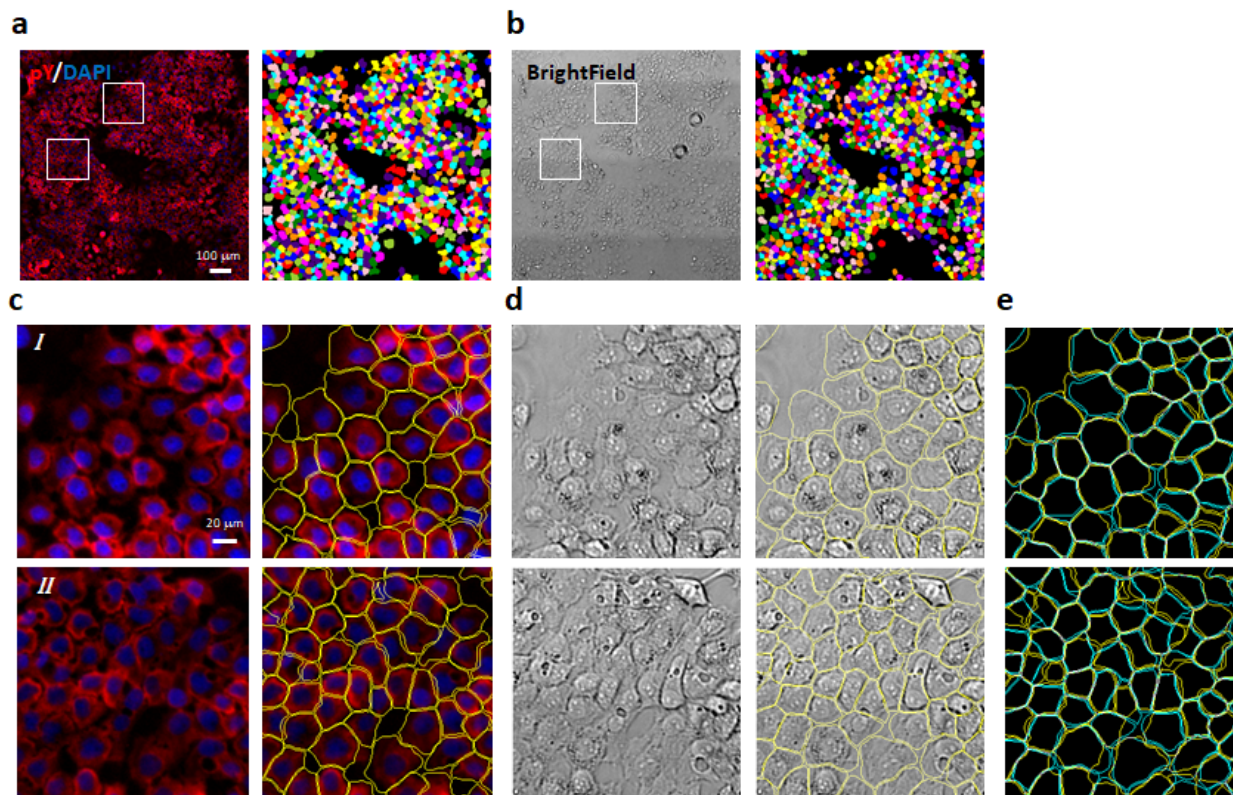


**Figure 2.** Segmentation of microscopy images by the CNN. Anti-pY immunofluorescence (a) and bright-field (b) images of A431 cells were acquired from the same sample location and the CNN segmentation results are shown as color maps (a and b, right panels). (c & d) Zoomed-in view of the segmentation results from the two subregions denoted by the white boxes in a & b. Here only the outline of the segmentations were plotted as image overlays (c & d, right columns). (e) Comparisons of the segmentation results based on the immunofluorescence images (yellow) versus the bright-field images (cyan). Data depict the same sub-regions as shown in c & d. All CNN segmentation models were trained with either the immunofluorescence image or the bright-field image only. DAPI images (shown in blue in a & c) were used for determining marker locations, but not used in training the CNN model.

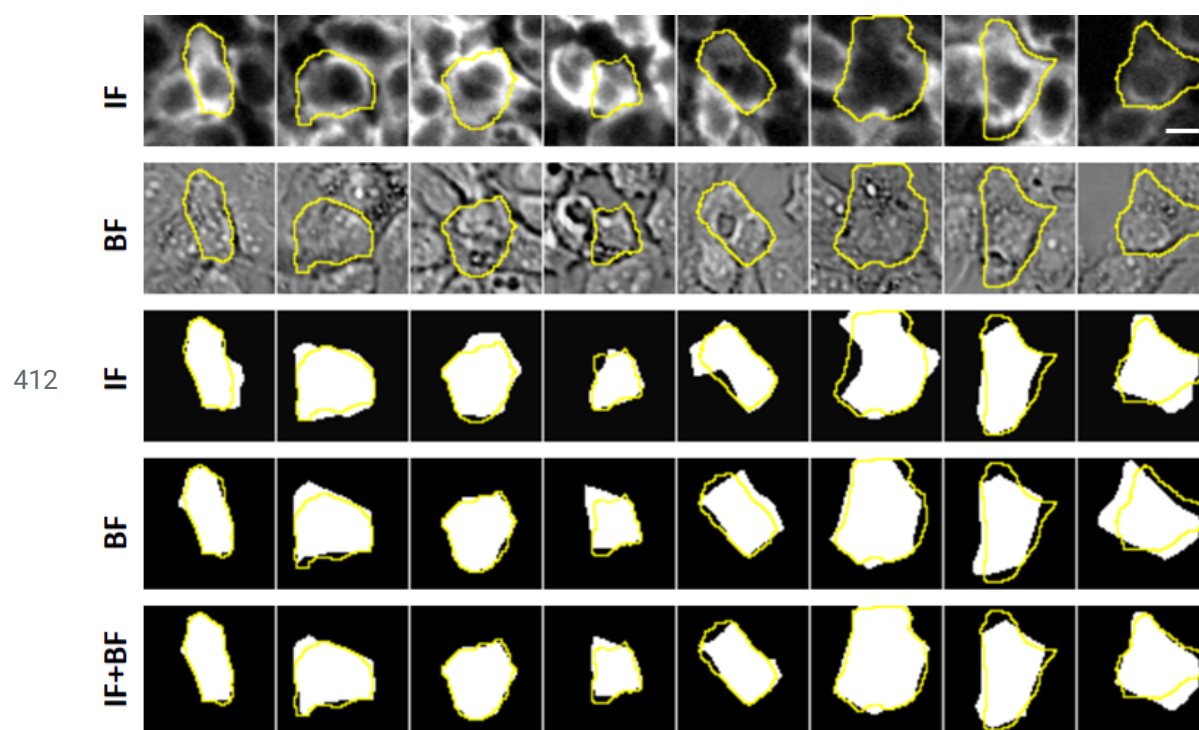


**Figure 3.** Comparisons between machine and manual segmentation results. Top two rows show the examples of individual image patches from the training data. The first row shows the patches from the anti-pY immunofluorescence (IF) images. The second row shows the patches from the bright-field (BF) images. The bottom three rows show the CNN segmentation output of each image patch. The models were trained with either the IF (row 3), BF (row 4) or multi-channel input of IF and BF combined (row 5). In all cases, the manual segmentations of the cells were plotted as the yellow overlays. Manual segmentation is based on a combined input of IF, BF and nucleus (DAPI) images (not shown here). The scale bar represents 20  $\mu\text{m}$ .

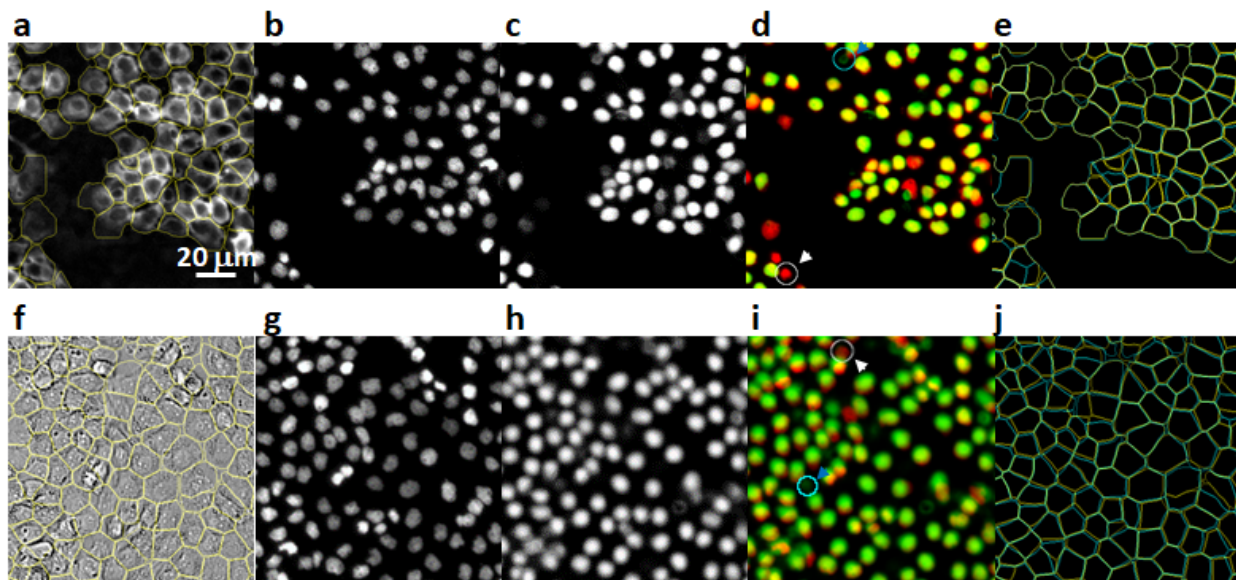


**Figure 4.** Segmentation based on synthetic marker locations. Results for the anti-pY immunofluorescence data are shown in panel **a-e**, and results for the bright-field image are shown in **(f-j)**. The input images (**a & f**) were shown together with the segmentation results (yellow overlay). Experimentally acquired nucleus (DAPI) images were shown in **b & g** for comparison, although they were not used for the computation of the segmentation. Instead, synthetic nucleus images (**c & h**) were computed directly from the input images (**a & f**) using a pre-trained CNN. Errors in the synthetic images can be easier discerned in the composite overlay images (**d & i**) of the experimental (red) and synthetic (green) nucleus images. Both false negative (white arrow) and false positive (blue arrow) errors were found, but are of relatively low occurrences. Finally, the segmentation results based on synthetic markers were compared with the “proper” segmentation, for which the experimental DAPI images were used for marker locations. The comparisons were shown in **e & j**, where segmentations based on experimental markers (yellow) were drawn in overlay on segmentations based on synthetic markers (cyan).

438

439 Table I. Unsupervised CNN segmentation accuracy.

440	Training Inputs	FLuorescence*	<input checked="" type="checkbox"/>	<input checked="" type="checkbox"/>	<input type="checkbox"/>	<input type="checkbox"/>	<input checked="" type="checkbox"/>	<input checked="" type="checkbox"/>
		BrighField	<input type="checkbox"/>	<input type="checkbox"/>	<input checked="" type="checkbox"/>	<input checked="" type="checkbox"/>	<input checked="" type="checkbox"/>	<input checked="" type="checkbox"/>
		Nucleus	<input type="checkbox"/>	<input checked="" type="checkbox"/>	<input type="checkbox"/>	<input checked="" type="checkbox"/>	<input type="checkbox"/>	<input checked="" type="checkbox"/>
	mIOU	CNN	0.779±0.026	0.809±0.012	0.710±0.017	0.766±0.040	0.765±0.43	<b>0.821±0.025</b>
		Cell Profiler	0.69					

\* anti-pY immunofluorescence images.

441

442

443



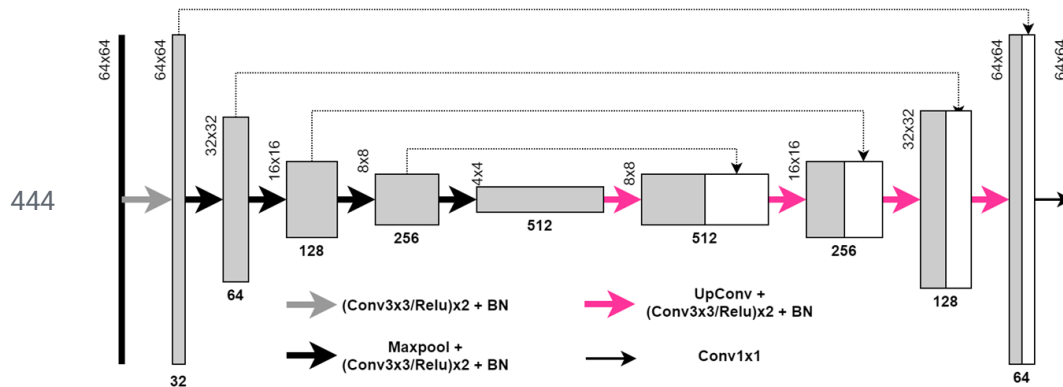


**Figure S1.** Architecture of the CNN used for segmentation. The encoder portion of the network extracts image features by multiple stages of convolution and max pooling. The decoder portion of the network constructs the segmentation by incremental upscaling of the feature map (to 2x larger dimension) followed by convolution. Feature map obtained in the decoding step is concatenated by intermediate results at the decoding steps in order to supplement feature information at incrementally higher resolution. Relu activation is used throughout the encoding and decoding steps, except in the final output layer, in which a sigmoid activation is used. The same network is used for producing synthetic nucleus images, in which case the input tensor dimension is much larger (870x870) to match the size of training data.

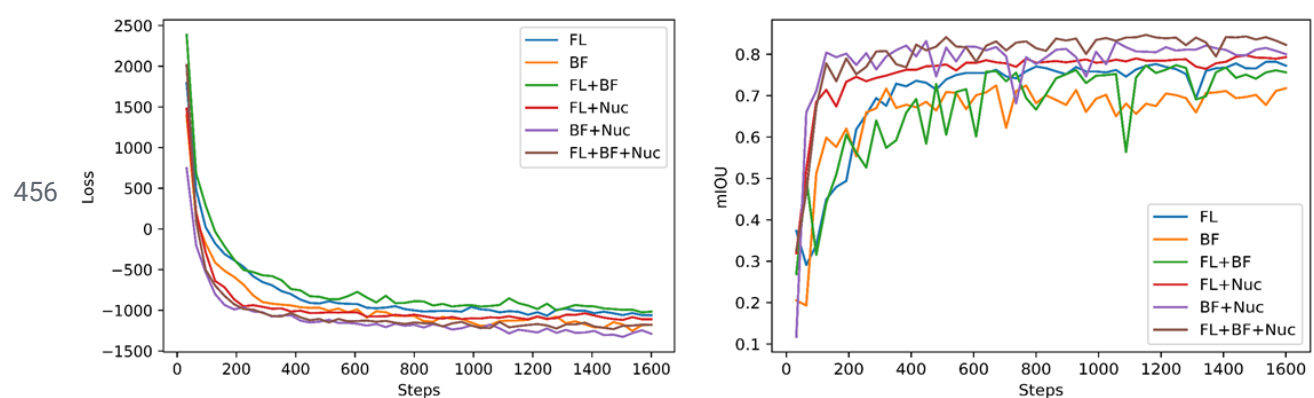


**Figure S2.** Representative training traces showing the minimization of the loss function (left) and the corresponding optimization of the segmentation accuracies (right) over the self-supervised training process. Multiple models were trained with various combinations of input data, including the immunofluorescence image (FL), the bright-field image (BF) and the DAPI staining image (Nuc).



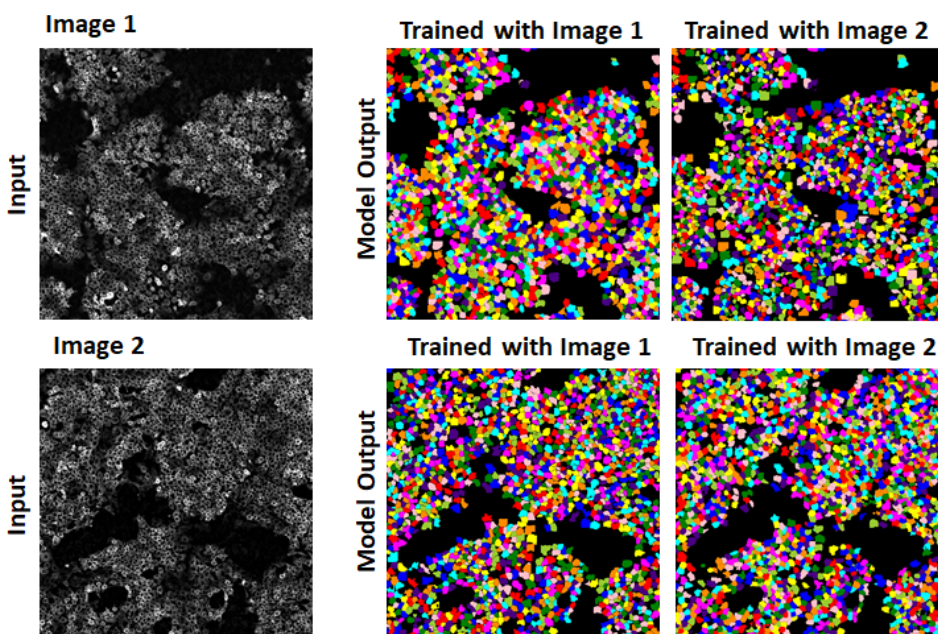


**Figure S3.** Comparison of segmentation results on both seen and unseen fluorescence images.

Two segmentation models were separately trained by two immunofluorescence images of the same modality (left) and the resulting models were used to operate on both images (one seen and one unseen) to obtain the segmentation (right). The results demonstrated that the models trained this way were able to apply learnings to unseen data of similar features.

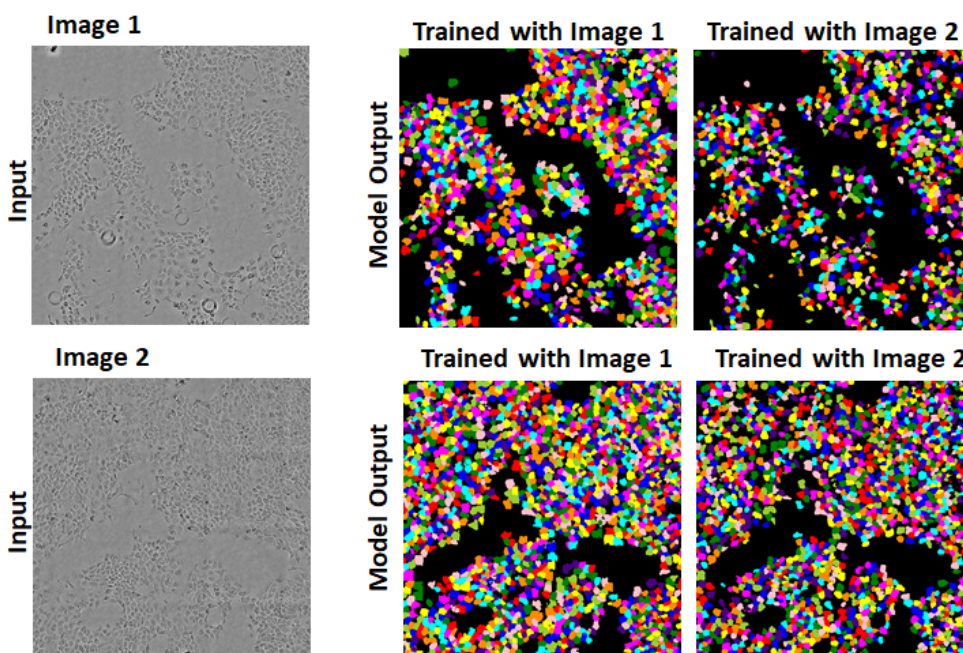


**Figure S4.** Comparison of segmentation results on both seen and unseen bright-field images.

This is the same analysis as in Fig S3 except on bright-field images.